J. Fluid Mech. (2001), *vol.* 446, *pp.* 229–252.
DOI: 10.1017/S0022112001005754 Printed in the United Kingdom

Interaction of unequal anti-parallel vortex tubes

By J. S. MARSHALL†, P. BRANCHER AND A. GIOVANNINI

Institut de Mécanique des Fluides de Toulouse,
Allée du Professeur Camille Soula 31400 Toulouse, France

(Received 25 January 2000 and in revised form 17 May 2001)

A computational study is reported of the close interaction of nominally anti-parallel vortex tubes with unequal strengths, Γ_1 and $-\Gamma_2$, where $\Gamma_2/\Gamma_1 \leqslant 1$. The computations are performed using a spectral method, with periodic boundary conditions and vortex Reynolds number $Re \equiv \Gamma_1/\nu = 1500$, and the vortices are perturbed by a wavelength for which the pair is unstable because of their mutual interaction. The numerical method is tested for the case of equal-strength vortices, which exhibits the classic vortex reconnection phenomenon typified by bridging between the vortex cores and formation of thin vorticity threads as the bridged sections advect away under their self-induced velocity. Computations for vortices of unequal strengths are reported for cases with small, moderate and large strength differences, for which $\Gamma_2/\Gamma_1 = 0.82$, 0.54 and 0.25 are chosen as representative values. The bridges between the vortex structures form loops that twist owing to the unequal vortex strengths. In the thread region, the vortex interaction is controlled by competition between the effects of stretching of the weak vortex as it wraps around the stronger vortex and the core distortion induced on each vortex owing to the straining imposed by the opposing vortex. For cases with large vortex strength difference, the strong vortex remains nearly straight as the weak vortex wraps around it, inducing an interlaced pattern of positive and negative vorticity spirals within the core of the strong vortex. Over long time, the bridge regions form loops that propagate away from the thread region for cases with small strength difference and wrap around the nearly columnar strong vortex for cases with large strength difference.

1. Introduction

The process by which two approaching vortices are cut and reconnect to each other has been of interest to the fluid dynamics community for several decades. This process has at various times been proposed as a key ingredient in the turbulence energy cascade (Kida & Takaoka 1994) and in generation of aerodynamic noise (Takai & Hussain 1985), and it is clearly important in controlling breakup of aircraft wake vortices under certain atmospheric conditions (Tombach 1973; Liu 1992). However, the main reason for interest in the vortex reconnection problem is perhaps more fundamental, arising from the fact that it is associated with a topological change in the vortical structures that underlie most fluid motions.

Previous work on vortex reconnection has principally focused on one of two

† Author to whom correspondence should be addressed: permanent address: Department of Mechanical Engineering, University of Iowa, Iowa City, IA 52242, USA.

geometrical configurations – the impact of two equal-strength vortex rings, in which the self-induced velocity of the rings drives the vortices together, and the interaction of two anti-parallel vortex tubes of equal strength, in which the vortices are driven together by their mutual instability. A review of research on vortex reconnection in general is given by Kida & Takaoka (1994). The interaction of anti-parallel vortex tubes is of particular interest since, as noted by Siggia (1985) and Zabusky & Melander (1989), vortex tubes with arbitrary initial orientation tend to become reoriented in an anti-parallel manner as they approach each other owing to their self- and mutually-induced velocity fields. Computational studies of equal-strength anti-parallel vortex tubes have been performed by Pumir & Kerr (1987), Melander & Zabusky (1988), Melander & Hussain (1989), and Shelley, Meiron & Orszag (1993), where the latter paper focuses on evaluation of a theoretical model of vortex reconnection due to Saffman (1990). From this work, a fairly clear understanding of the physical processes of reconnection of equal-strength vortices has arisen, which we review in § 3 of the paper.

With the notable exception of aircraft wake vortices, interacting vortices in nature are rarely of equal strength. Indeed, the interaction of vortices of very different strength is central to understanding vortex dissipation at high Reynolds number, as illustrated in the direct numerical simulation of vortex interaction with surrounding turbulence by Melander & Hussain (1993) and the experimental work on decay of airfoil trailing vortices subjected to surrounding turbulence by Bandyopadhyay, Stead & Ash (1991). This problem is fundamental to development of more physically grounded models for turbulence cascade processes and for subgrid-scale models used in large-eddy turbulence simulation. On a more practical basis, understanding of the interaction of vortices of different strengths may be useful for control of vortical flows. For instance, one approach to enhance dissipation of aircraft trailing vortices is to introduce nearby weaker vortices with opposite-sign vorticity, which might be generated by spoilers, flaps or other control devices (Corsiglia & Dunham 1976; Croom 1976; Quackenbush *et al.* 1997, 1998). In future aircraft, it may even be possible to actively perturb the weaker vortex so as to enhance its interaction with the principal wake vortex. Similar control techniques might also be effective for suppression of coherent structures in turbulent boundary layers, where the secondary vortices may be produced by localized blowing (Acarlar & Smith 1987) or by small control surfaces attached to the boundary.

A stability analysis for anti-parallel vortices of unequal strength is given by Klein, Majda & Damodaran (1995), which extends the classic Crow (1970) theory for equal-strength vortices. Previous investigations focusing on the core dynamics during close interaction of vortices of unequal strength have been performed for various geometrical configurations, including computations of the impact of a vortex pair on an orthogonally offset vortex (Zabusky & Melander 1989), the wrapping of an initially elliptical vortex around a columnar vortex (Krishnamoorthy & Marshall 1998), and the axisymmetric interaction between periodic vortex rings and a columnar vortex placed along the symmetry axis (Marshall 1997). These previous studies suggest some of the physical features of the vortex response to this interaction, including deformation of the core cross-section, wrapping of the weak vortex around the strong, and (in some cases) ejection of vorticity from the strong vortex.

This paper presents a study of the effect of strength difference on interaction of anti-parallel vortex tubes, focusing on the core dynamics as the vortices impact upon each other. A description of the numerical method and checks of grid and time step resolution are described in § 2. The problem of vortex reconnection for equal-

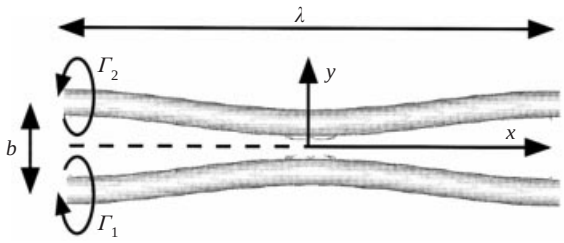

FIGURE 1. Diagram showing initial configuration of the vortex tubes, with wavelength λ, nominal separation distance b, and strengths Γ_1 and $-\Gamma_2$.

Identification	Γ_2/Γ_1	σ_2/σ_1	λ	Δt
A	1	1	7.3	0.10
B	0.82	1	7.2	0.10
C	0.54	1	7.0	0.10
D	0.25	1	6.2	0.08
E	0.25	0.5	6.2	0.08

TABLE 1. Summary of computational parameters for different runs.

strength anti-parallel vortices is reviewed in § 3. The vortex reconnection problem for unequal-strength vortex pairs is examined in §§ 4–6 for values of the strength ratio Γ_2/Γ_1 ranging from near unity (slight strength differences) to near zero (large strength differences). The vortex reconnection process is found to be significantly modified as Γ_2/Γ_1 is decreased from unity, even for slight differences in the vortex strengths. The long-time evolution of the vortices is examined in § 7, for a case with slight difference in vortex strength and another with large strength difference. Conclusions are presented in § 8.

2. Numerical method

Numerical computations are performed on a cubic domain with 128^3 grid points and periodic boundary conditions. A schematic of the vortex initial condition is shown in figure 1. All variables are non-dimensionalized using the nominal vortex separation distance b and the inverse of the maximum vorticity of the unperturbed strong vortex to determine length and time scales. The initial vorticity profile is Gaussian with radial length scale $\sigma_1 = 0.2$ for the strongest vortex. The vortices are initially symmetrically perturbed at angles of $\pm 45^\circ$ with amplitude $A_0 = 0.2$. The length λ of the periodic computational domain is chosen such that the vortex pair is unstable according to the three-dimensional linear stability theory (Klein *et al.* 1995). The parameters used in the various cases considered, denoted A–E, are summarized in table 1. All computations are performed for a vortex Reynolds number $Re = \Gamma_1/\nu = 1500$.

A pseudo-spectral method is used with second-order Adams–Bashforth time stepping, which is dealiased using the standard two-thirds wavenumber truncation. The spectral Navier–Stokes equations are evolved in time after having been projected onto a divergence-free space using the operator $P_{ij} = k_i k_j/k^2 - \delta_{ij}$ and with exact time integration of the viscous term, according to the expression

$$\hat{\boldsymbol{u}}_{n+1} = \hat{\boldsymbol{u}}_n \exp(-\nu' k^2 \Delta t) + \Delta t \boldsymbol{P} \cdot [\tfrac{3}{2}(\boldsymbol{u}\times\boldsymbol{\omega})_n \exp(-\nu' k^2 \Delta t) - \tfrac{1}{2}(\boldsymbol{u}\times\boldsymbol{\omega})_{n-1} \exp(-2\nu' k^2 \Delta t)] \quad (1)$$

where $\boldsymbol{u}$ and $\boldsymbol{\omega}$ are the velocity and vorticity vectors, a top hat denotes Fourier transform, a subscript indicates the time step, and $\nu' \equiv \pi\sigma_1^2/Re$. The time step is held fixed during the computations at $\Delta t_0 = 0.002\lambda^2$, such that the CFL number, $u_{max}\Delta t/\Delta x$, is less than 0.15 for all cases considered. The computations are initialized by specifying a vorticity field and taking its Fourier transform, and then inverting the spectral form of the vorticity definition $\hat{\boldsymbol{\omega}} = \mathrm{i}\boldsymbol{k} \times \hat{\boldsymbol{u}}$ to obtain $\hat{\boldsymbol{u}}$. The computations were performed on a Cray T-90 and require about 3.2 CPU seconds per time step.

These computations are intended to describe the evolution of two nominally anti-parallel vortices subject to periodic perturbations in the axial direction. The neighbouring periods of the flow in the transverse directions are a consequence of the use of Fourier decomposition in the numerical method. The computational domain is a cube with length λ in all directions, where λ varies between 6.2 and 7.3 for the different computations. The transverse length scale for vortex interaction during the initial instability of the pair is the nominal distance between the vortices, $b = 1$. For the part of the computation during which the weak vortex impinges upon and partially reconnects with the core of the stronger vortex, the typical transverse length scale is equal to the vortex radius, $\sigma_1 = 0.2$, which is smaller than the side length of the cubic domain by a factor of over 30. Thus, although the neighbouring periods of the flow in the transverse directions may have some small effect on the growth rate during the initial vortex instability, it is unlikely that they have a discernable influence on the core dynamics during close interaction of the vortices, which is the principal focus of the current paper.

Calculations with $\Gamma_2/\Gamma_1 = 0.54$ (case C) are repeated with 64^3 grid points and a time step of $\Delta t = 2\Delta t_0$ in order to verify grid and time-step independence of the computed results. This case was chosen as typical of the computations with unequal vortex strength. One measure of the sensitivity of the computations to choice of grid size or time step is given by comparing the variation of global flow measures for computations with different resolution. For instance, the enstrophy E, defined by

$$E = \tfrac{1}{2}\int_V \boldsymbol{\omega}\cdot\boldsymbol{\omega}\,\mathrm{d}v, \tag{2}$$

where V denotes the computational domain, increases owing to vorticity stretching and decreases under the action of viscous dissipation. Previous investigators have reported substantial decrease in enstrophy during reconnection of symmetric vortices (Kida & Takaoka 1994). Enstrophy variation over time is shown in figure 2 for both the high resolution 128^3 case and the medium resolution 64^3 case. The enstrophy decreases by a factor of nearly 10 during the computation and exhibits close agreement between the 64^3 and 128^3 cases.

Another test of the computational resolution is to plot time variation of global quantities that are supposed to remain invariant during the computation. Among these, we consider in particular the total circulation Γ_{tot} over the symmetry plane $x = 0$ and the integral V_x of vorticity in the x-direction over the entire flow field, defined by

$$\Gamma_{tot} = \int_{-\lambda/2}^{\lambda/2}\int_{-\lambda/2}^{\lambda/2}\omega_x(0,y,z)\,\mathrm{d}y\,\mathrm{d}z, \quad V_x = \int_V \omega_x\,\mathrm{d}v. \tag{3}$$

A plot of time variation of Γ_{tot} and V_x are given in figure 3 for both (*a*) the 128^3 case and (*b*) the 64^3 case. In the 128^3 case, V_x decays by about 4% during the computation and Γ_{tot} is observed to fluctuate slightly, with maximum deviation of about 3% of the average value. These results suggest that the grid is sufficiently fine that numerical

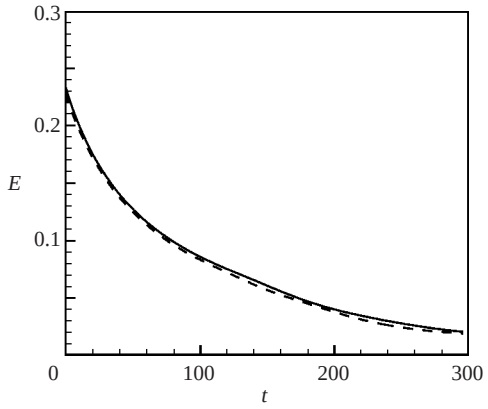

FIGURE 2. Variation of enstrophy with time for case C, showing results for computations with ——, 128^3 grid and $\Delta t = \Delta t_0$ and - - -, with 64^3 grid and $\Delta t = 2\Delta t_0$.

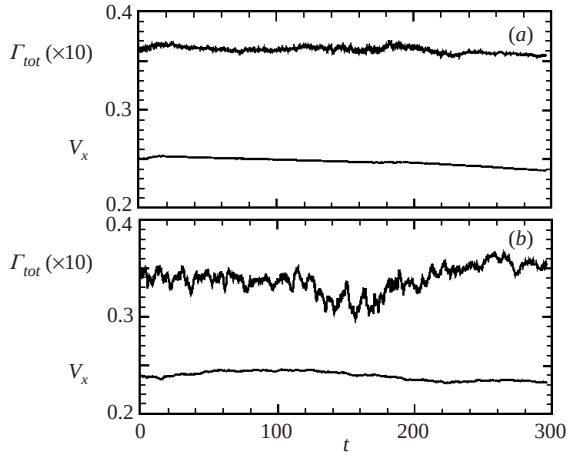

FIGURE 3. Time variation of the total circulation in the $x = 0$ symmetry plane and the integral of ω_x over the computational domain, for computations with (*a*) 128^3 grid and $\Delta t = \Delta t_0$ and (*b*) with 64^3 grid and $\Delta t = 2\Delta t_0$.

dissipation of vorticity is small during the computations. Sensitivity of these measures on grid resolution can be evaluated by examining the results for the 64^3 case, for which V_x is again fairly constant but much greater fluctuations of Γ_{tot} are observed, with deviations of up to 15%.

3. Reconnection of equal-strength vortices

A computation of reconnection of equal-strength vortex tubes (case A) is performed in order to establish a basis for comparison for cases with unequal vortex strengths. A time series showing the vortex interaction during reconnection is given in figure 4, in which the λ_2-technique of Jeong & Hussain (1995) is used to identify the boundary of the vortex structures. In figure 4, and in other figures using this technique in the remainder of the paper, we plot iso-surfaces with $\lambda_2 = -0.0002$, where λ_2 is the middle eigenvalue of the symmetric tensor with components $H_{ij} = S_{ik}S_{kj} + \Omega_{ik}\Omega_{kj}$. Here, S_{ij} and Ω_{ij} are the components of the deformation rate tensor and the vorticity tensor,

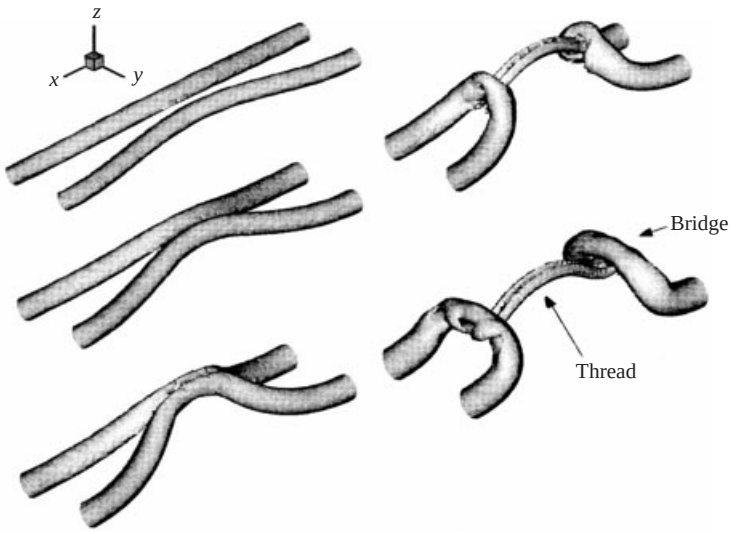

FIGURE 4. Iso-surface of λ_2 for symmetric vortex reconnection (case A) at times $t = 0$, 53, 107, 160 and 213.

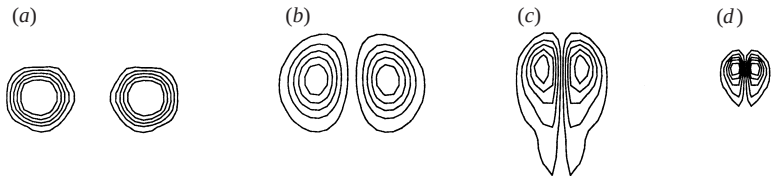

FIGURE 5. Contours of ω_x in the $x = 0$ symmetry plane for the first four times shown in figure 4.

respectively. If the vorticity vanishes at any point, the tensor $\boldsymbol{H}$ is positive definite and all of its eigenvalues are positive. Iso-surfaces with negative value of λ_2 therefore lie within the vorticity-containing part of the flow. Plots with other small negative values of λ_2 exhibit similar structural forms to those given in figure 4. Vorticity contours in the $x = 0$ symmetry plane at four times are shown in figure 5, corresponding to the first four frames of figure 4.

The vortex interaction illustrated in figures 4 and 5 exhibits the classic vortex reconnection stages, as described by several previous authors (e.g. Melander & Hussain 1989, Kida & Takaoka 1994). The vortex perturbations first grow as predicted by the unstable symmetric mode of the Crow (1970) instability analysis. The vorticity contours within the core become increasingly deformed as the vortices move toward each other, developing into the head-trail structure shown in figure 5(*c*). This stage is characterized by active cross-diffusion, which by necessity is accompanied by bridging between the two vortex structures as a consequence of the requirement that the strength of a vortex tube remains constant. As the bridges linking the two vortex tubes begin to form, their self-induced velocity causes them to propagate upward and away from each other. Because of this motion of the bridges, the vorticity cross-diffusion between the two structures does not have a chance to completely annihilate the vorticity in the central region. The remnants of vorticity as the bridges pull away from each other, called the threads, arc upward owing to the velocity induced by the bridges. The curvature of the threads leads to a self-induced velocity driving them away from each other. The velocity induced by the bridges also causes strong

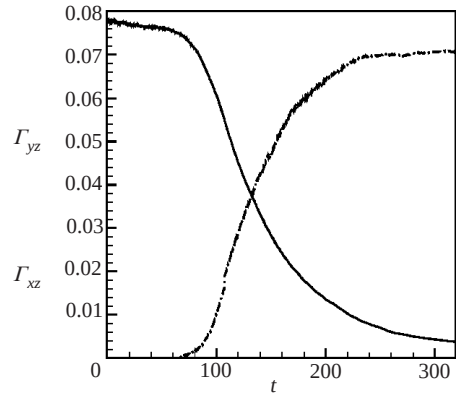

FIGURE 6. Time variation of circulation in the (y, z)- and (x, z)-half-planes for symmetric vortex reconnection.

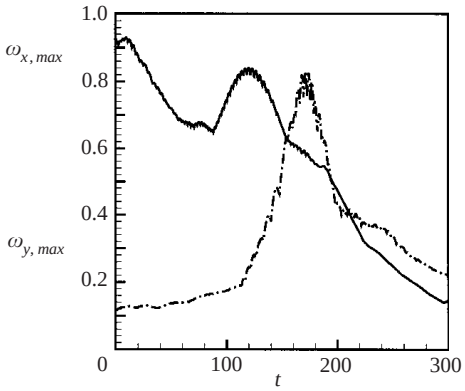

FIGURE 7. Time variation of the maximum vorticity values in the x- and y-directions for symmetric vortex reconnection.

stretching of the threads, which intensifies the vorticity within the thread cores and introduces a radial inflow that counters their self-induced velocity. Consequently, the threads appear to remain in contact but the cross-diffusion between them is slow.

One way of quantifying the reconnection process is to plot the time variation of circulation in half of the (y, z)- and (x, z)-symmetry planes, denoted by Γ_{yz} and Γ_{xz}, as shown in figure 6. The circulation in the (x, z)-plane is initially zero and that in the (y, z)-plane is nearly constant in time as the vortices advect towards each other. A sudden drop in Γ_{yz} occurs at a time of about 80, with a corresponding increase in Γ_{xz}, as the vortices move sufficiently close together that active cross-diffusion can occur. At a time of around 200, most of the bridging has been completed and the two vortex loops advect away from each other, leaving the threads behind. For times later than about 280, Γ_{yz} and Γ_{xz} remain fairly constant, although there is a gradual decrease of Γ_{yz} because of diffusion between the threads.

While the vorticity magnitude generally decreases under the action of viscous diffusion during the computation, it is observed in figure 7 that peak values of both ω_x and the transverse vorticity, represented by ω_y, occur owing to vortex stretching during the bridging process. The peak in ω_x occurs during the early part of the reconnection as the bridges are being formed. The peak in ω_y occurs later, after

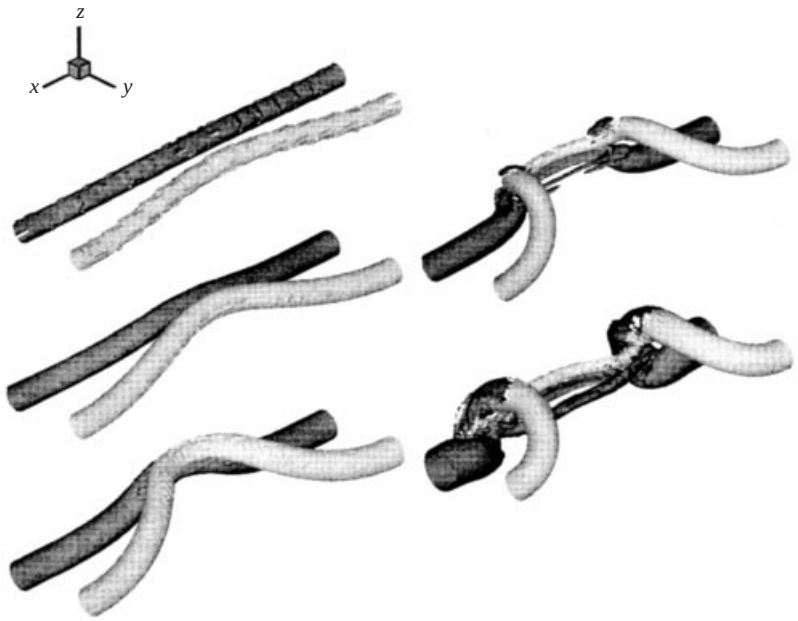

FIGURE 8. Series of iso-surfaces of λ_2 for case B at times $t = 0$, 52, 104, 156 and 207. The surfaces are shaded dark grey for $\omega_x > 0$ and light grey for $\omega_x < 0$.

the bridges have formed and are starting to pull away from each other. Following reconnection, both vorticity measures decay significantly.

4. Interaction of vortices with small strength differences

When the vortex strength is not equal, the symmetry between the two vortex tubes over the (x, z)-plane is broken. The resulting asymmetry can significantly alter the nature of the vortex reconnection, even for fairly slight vortex strength differences. The effects of this asymmetry are examined in the current section using computations of vortex interaction with $\Gamma_2/\Gamma_1 = 0.82$ (case B). This interaction is illustrated using a time series of iso-λ_2 surfaces in figure 8, with corresponding plots of contours of ω_x in the $x = 0$ symmetry plane given in figure 9. In order to help distinguish between the two vortex structures, the iso-λ_2 surfaces are shaded dark grey for points with positive ω_x and light grey for points with negative ω_x. The vorticity contour plots in figure 9 are shaded grey for negative values of ω_x, corresponding to the weak vortex. Use of this shading scheme to identify from which vortex the vorticity originates should be employed with care during the late stages of the vortex interaction, both because the vortex with negative ω_x may fold back in the positive x-direction and because it is not clear how to identify vorticity motion in three-dimensional flows with strong diffusion (see Kida & Takaoka 1994, for further discussion of this point).

Even for this small strength difference, the weak vortex is observed to wrap around the strong vortex with only modest bending of the strong vortex, which is in qualitative agreement with the vortex filament computations reported by Klein *et al.* (1995). The instability thus leads to a large amount of stretching within the central part of the weak vortex, but much less within the strong vortex. During the initial part of the interaction, the core cross-section of both the weak and strong vortices deform in a nearly symmetric manner owing to the straining induced by the opposing

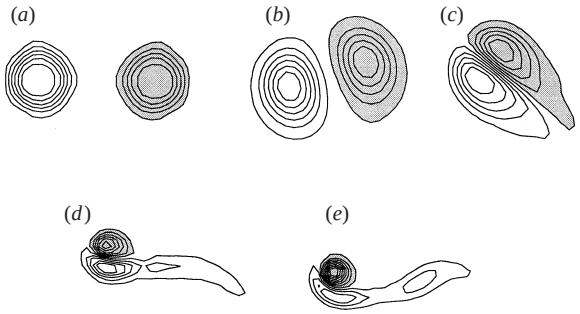

FIGURE 9. Contours of ω_x in the $x = 0$ symmetry plane for the same times as shown in figure 8. Contours with negative values are shaded.

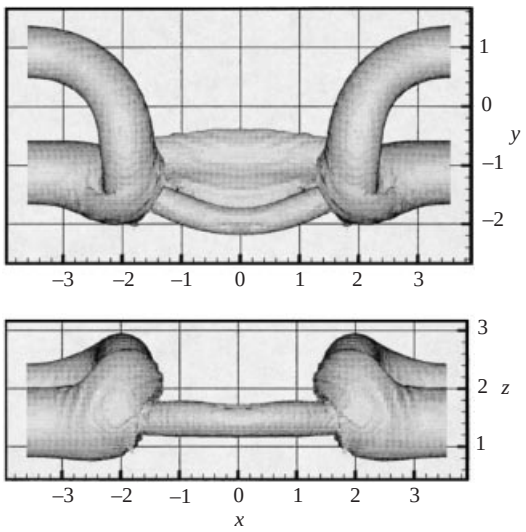

FIGURE 10. Iso-surface of vorticity magnitude ($\omega = 0.02$) for case B at time $t = 207$, showing projections in the (x, y)- and (x, z)-planes.

vortex. We might expect that the strong vortex would eventually be victorious in this contest as the vortices are driven increasingly close together, and that the weak vortex core would be torn apart after sufficiently long time. Surprisingly, the computations indicate that for small vortex strength differences, just the opposite occurs. While the total strength of the weak vortex is less, the vorticity magnitude within the weak vortex core becomes greater than that within the strong vortex owing to the large amount of stretching associated with the vortex instability and the resulting wrapping of the weak vortex about the strong vortex. Hence, it is the weak vortex that at long times maintains a coherent, nearly circular, shape and the strong vortex whose core is deformed into an elongated sheet, as shown in the final frames of figures 8 and 9.

The iso-λ_2 plots are useful for presenting the motion of the dominant vortex structures during the interaction; however, they lose some of the detail of the vorticity field when it becomes highly deformed. Iso-surface plots of vorticity magnitude are therefore used to provide an alternative view of the vorticity field in the late stages of the interaction, where the threshold value $\omega = 0.02$ is used for all such plots presented in the paper. The vorticity magnitude iso-surface for case B at time $t = 207$ is shown in figure 10, with projections in both the (x, y)- and (x, z)-planes. In the top view in

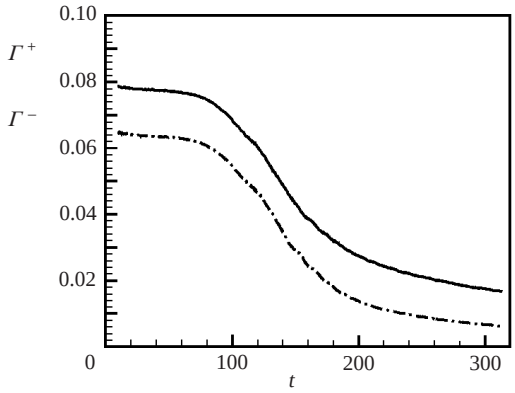

FIGURE 11. Time variation of the circulation measures Γ^+ and Γ^- in the $x = 0$ symmetry plane for case B.

figure 10 ((x, y)-plane), the weak vortex is observed to bend down and connect to the strong vortex, leaving a coherent thread of vorticity with nearly circular core connecting the two half loops. The broad region of vorticity on top of this thread is the deformed remnant of the strong vortex.

To quantify the vorticity cross-diffusion during the interaction, we plot in figure 11 time variation of two circulation measures, Γ^+ and Γ^-, obtained by integrating over the entire $x = 0$ symmetry plane the vorticity for all points with positive and negative values of ω_x, respectively. As in the case of symmetric reconnection, the circulation measures remain nearly constant during the first part of the interaction as the vortices advect toward each other, decrease rapidly during the second part of the interaction in which cross-diffusion is active, and then decay gradually during the final part of the interaction as the reconnected loops advect away from the $x = 0$ symmetry plane. The negative circulation measure does not go to zero, at least not during the length of the current computation, so the highly asymmetric thread structures remaining have x vorticity components of both positive and negative signs. The difference between the initial and current values of Γ^+ is equal to the strength of the vorticity bridge connecting the two vortices at a given time.

The maximum vorticity values in the x- and y-directions are plotted as functions of time in figure 12. Both vorticity components exhibit local peaks during the vortex interaction, at approximately the same times as for the symmetric reconnection case. However, both peak values are significantly smaller than in the symmetric case. The y-vorticity in particular increases only to a value of about 0.4, which is about half of the peak value for the symmetric reconnection.

5. Interaction of vortices with moderate strength differences

As the difference in strength between the two vortices increases, the part of the weak vortex that wraps around the strong vortex becomes increasingly less able to withstand the core straining induced by the stronger vortex. We classify the interaction as one of moderate strength difference when the weak vortex core is eventually deformed by the stronger vortex, but it is still strong enough to simultaneously inflict serious deformation of the strong vortex.

An example of vortex interaction with moderate strength difference is given by the case with $\Gamma_2/\Gamma_1 = 0.54$ (case C). A time series of plots showing iso-λ_2 surfaces and

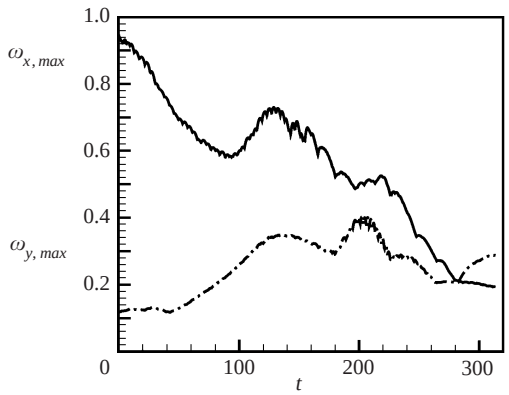

FIGURE 12. Time variation of the maximum vorticity values in the x- and y-directions for case B.

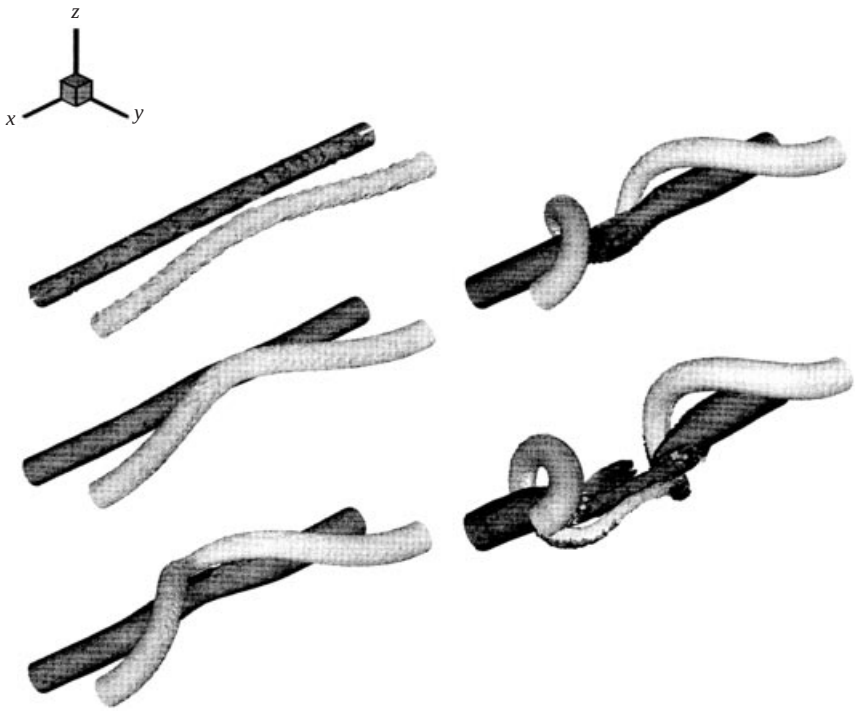

FIGURE 13. Series of iso-surfaces of λ_2 for case C at times $t = 0$, 49, 98, 147 and 196.

contours of ω_x in the $x = 0$ symmetry plane are given in figures 13 and 14. The vortex instability results in wrapping of the weak vortex around the strong vortex, with deformation of both vortex cores as the vortices move close to each other. While the vorticity within the weak vortex core is enhanced by the stretching associated with the wrapping process, it is also decreased by rapid cross-diffusion with the strong vortex. At long times, the main part of the weak vortex connects to the strong vortex core in a series of twisted loops. This connection is best observed from the plot in figure 15, which shows the projections of an iso-surface of vorticity magnitude at time $t = 245$ in the (x, y)- and (x, z)-planes. Of the remaining vorticity near the central part of the computational domain, the weak vortex core eventually becomes weak and elongated

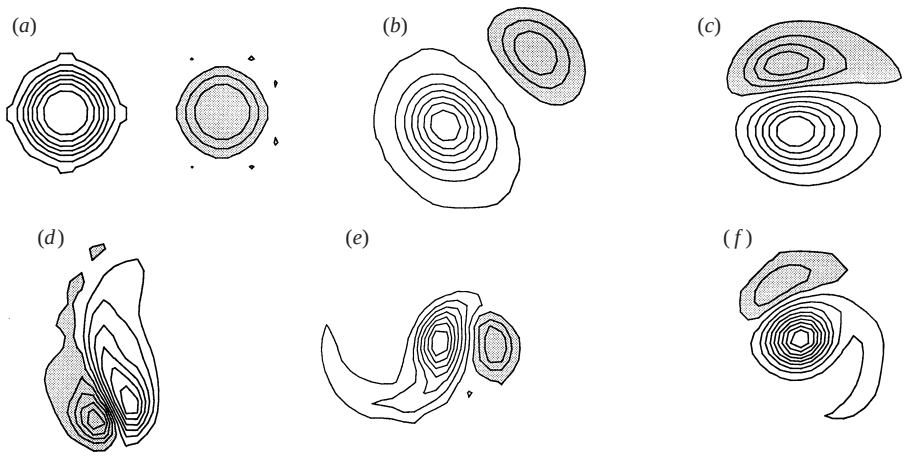

FIGURE 14. Contours of ω_x in the $x = 0$ symmetry plane for case C at times $t = 0$, 49, 98, 147, 196 and 245. Contours with negative values are shaded.

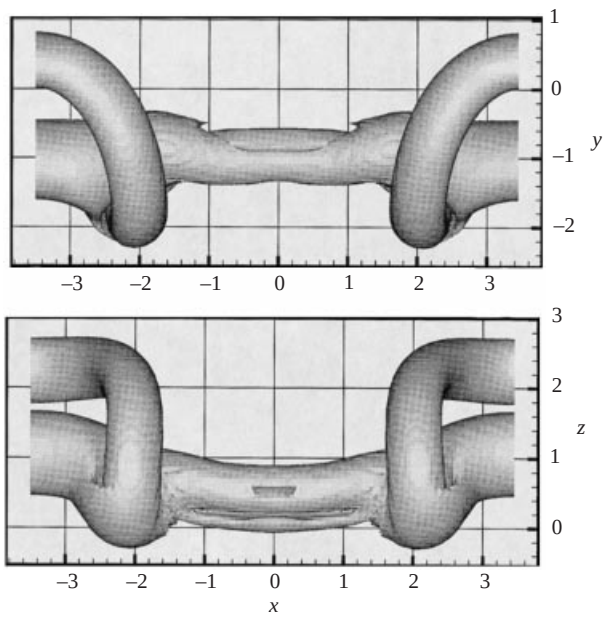

FIGURE 15. Iso-surface of vorticity magnitude ($\omega = 0.02$) for case C at time $t = 245$, showing projections in the (x, y)- and (x, z)-planes.

while that of the strong vortex rolls into a coherent tube-like structure. Vorticity that has been ejected from the strong vortex during this interaction spirals behind as a vorticity sheet.

Since at time $t = 245$ the projection of the strong vortex appears to be approximately straight in the (x, y)-plane, it is possible to examine the vorticity response within the strong vortex core by plotting vorticity components on a cross-section at $y = -1$, which slices nearly through the centre of the strong vortex. Contours of the vorticity component ω_x in the nominal axial direction and the vorticity component ω_y normal to the cross-sectional plane are shown in figure 16, where grey

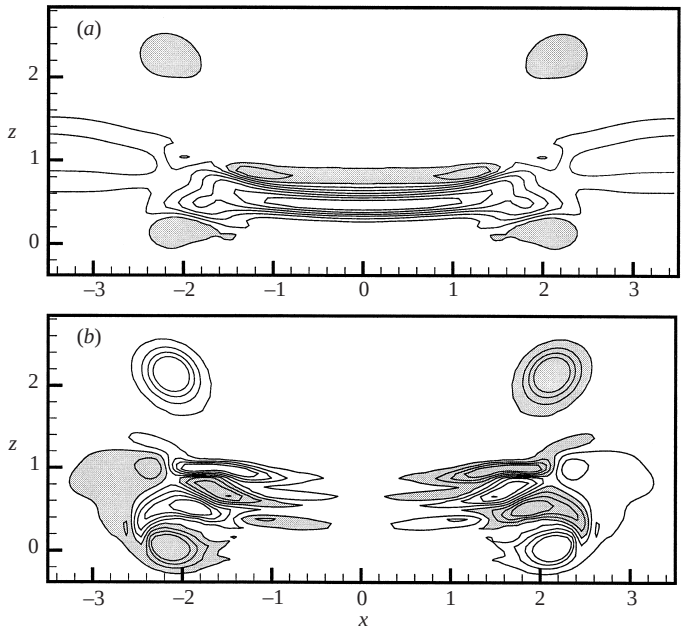

FIGURE 16. Contours of (*a*) ω_x and (*b*) ω_y over a planar cut at $y = -1$ for case C at time $t = 245$. Contours with negative values are shaded.

shading indicates negative contours. In figure 16(*a*), shaded contours of ω_x identify the location of the weak vortex, whereas unshaded contours fall within the strong vortex core. In figure 16(*b*), the ω_y contours indicate a series of oppositely signed patches as we proceed vertically from top to bottom on either side. By comparing with the top plot, we see that the outermost patches are due to the wrapping of the weak vortex. However, in the inner part of this alternating series we find generation of ω_y patches with sign opposite to that of the nearby weak vortex cross-section. As discussed by Marshall (1997), the generation of azimuthal vorticity (associated with ω_y) within the strong vortex plays an important role in regulating the vortex response to external straining exerted by the weak vortex as it wraps around the strong vortex core. The velocity induced by the weak vortex attempts to strip vorticity from the strong vortex core, whereas the azimuthal vorticity within the strong vortex attempts to restore the core to a state of uniform cross-sectional area. In the axisymmetric model system examined by Marshall (1997), it is found that forcing by the wrapped vortex structures results only in periodic standing waves on the strong vortex if the wrapped vortices are weak enough that their straining can be countered by the azimuthal vorticity generated within the strong vortex core. On the other hand, when the wrapped vortex structures are sufficiently strong, vorticity will be stripped from the core of the strong vortex in thin sheets. The mechanism responsible for generation of azimuthal vorticity within the core is described in § 6.

Time variation of the circulation measures Γ^+ and Γ^- on the $x = 0$ symmetry plane is plotted in figure 17. The three phases of reconnection phenomena – advection, bridging and threading – are still clearly detectable in the circulation plots, as in the symmetric reconnection case. The strong vortex circulation Γ^+ levels out at a value, that is approximately half of its initial value, and the weak vortex circulation Γ^-

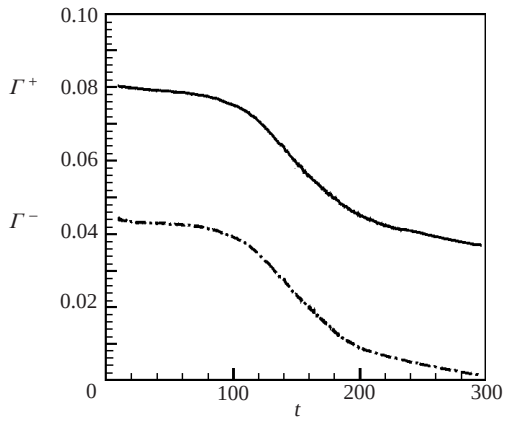

FIGURE 17. Time variation of the circulation measures Γ^+ and Γ^- in the $x = 0$ symmetry plane for case C.

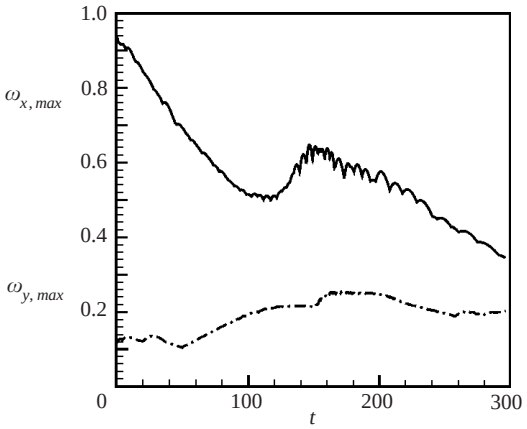

FIGURE 18. Time variation of the maximum vorticity values in the x- and y-directions for case C.

decays nearly to zero near the end of the computation, indicating that cross-diffusion has completely eliminated the weak vortex on the $x = 0$ symmetry plane.

Time variation of the maximum x and y vorticity components is plotted in figure 18. The x-component exhibits a small local maximum near time 160, after which it steadily decays. The y-component increases gradually during the first part of the computation to about twice its initial value, after which it remains approximately constant. Somewhat surprisingly, the vortex wrapping process does not exhibit the large vorticity increases that are characteristic of a flow with strong stretching, even compared to the symmetric reconnection case. Vortex interaction with moderate to small values of Γ_2/Γ_1 appears instead to be dominated by the processes of vorticity cross-diffusion and the quasi-two-dimensional deformation of the vortex cores, and although stretching certainly is not small enough to be negligible, its role in the interaction seems to become progressively less important as Γ_2/Γ_1 is decreased. It is not clear to what extent this result is influenced by the choice of Reynolds number and vortex core radius and whether it would continue to hold for vortex interaction at much higher Reynolds numbers or with large differences in core radius.

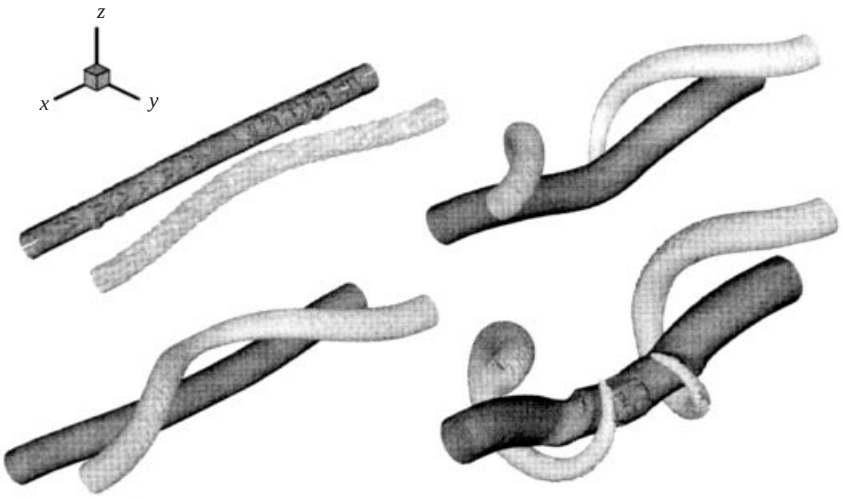

FIGURE 19. Series of iso-surfaces of λ_2 for case D at times $t = 0$, 77, 154 and 231.

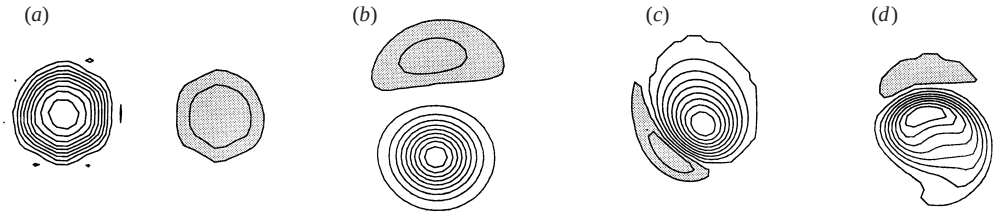

FIGURE 20. Contours of ω_x in the $x = 0$ symmetry plane for the same times as shown in figure 19. Contours with negative values are shaded.

6. Interaction of vortices with large strength differences

For cases with large differences in strength between the two vortex structures, the weak vortex becomes but a minor perturbation to the large vortex. This case is of primary interest for potential vortex control applications, in which it is desired to trigger breakup of a strong vortex structure by injection of weak nearby vortices. If such a control method is shown to be reasonable, it could be employed in applications as diverse as breakup of aircraft wake vortices to disruption of the coherent turbulent structures responsible for turbulence production in wall boundary layers or entrainment in fluid jets.

A computation showing anti-parallel vortex interaction with large strength difference is reported for $\Gamma_2/\Gamma_1 = 0.25$ (case D). This choice for vortex strength ratio was guided in part by the fact that the weak vortex becomes unstable to two-dimensional perturbations in the initial configuration for $\Gamma_2/\Gamma_1 < 0.14$. For values of Γ_2/Γ_1 below this limit, the ratio of strain rate induced by the strong vortex at the position of the weak vortex centreline to the vorticity of the weak vortex exceeds 0.15, which is the limiting value for existence of a steady-state solution for a uniform vorticity patch (Moore & Saffman 1971). Computations with values of Γ_2/Γ_1 above this limit would therefore be sensitive to the amplitude of the initial vortex perturbation, which determines the time required for development of the three-dimensional vortex pair instability.

The vortex interaction for case D is illustrated in the plots of iso-λ_2 surfaces and

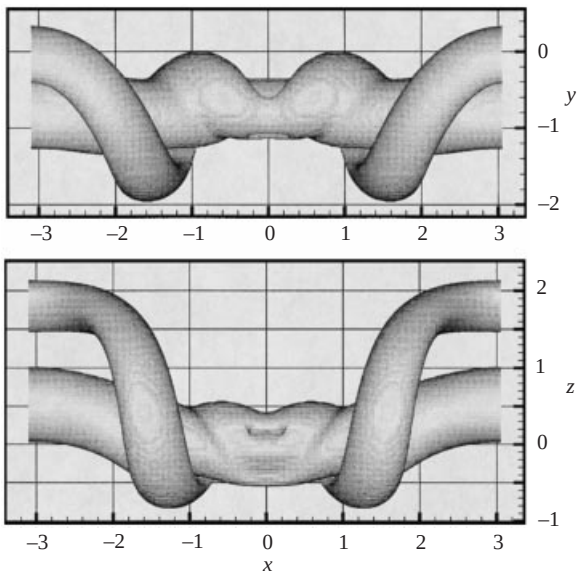

FIGURE 21. Iso-surface of vorticity magnitude ($\omega = 0.02$) for case D at time $t = 231$, showing projections in the (x, y)- and (x, z)-planes.

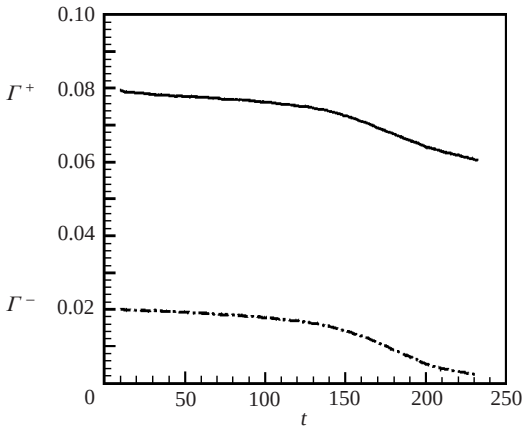

FIGURE 22. Time variation of the circulation measures Γ^+ and Γ^- in the $x = 0$ symmetry plane for case D.

the contours of ω_x in the $x = 0$ symmetry plane in figures 19 and 20, respectively. The weak vortex core elongates and its strength is reduced by cross-diffusion as it approaches and wraps around the strong vortex. By contrast, the strong vortex core remains nearly circular in cross-section, with only slight bending and cross-sectional deformation. Another view of the late stage of vortex interaction is given in figure 21, which shows prospective views of an iso-surface of vorticity magnitude at time $t = 231$ in the (x, y)- and (x, z)-planes. The weak vortex core is seen as a flattened structure that wraps around and attaches to the core of the strong vortex.

Time variation of the circulation measures Γ^+ and Γ^- in the $x = 0$ symmetry plane is shown in figure 22. The circulation measures decay more gradually than for cases with nearly equal vortex strength, which is a consequence of the fact that in

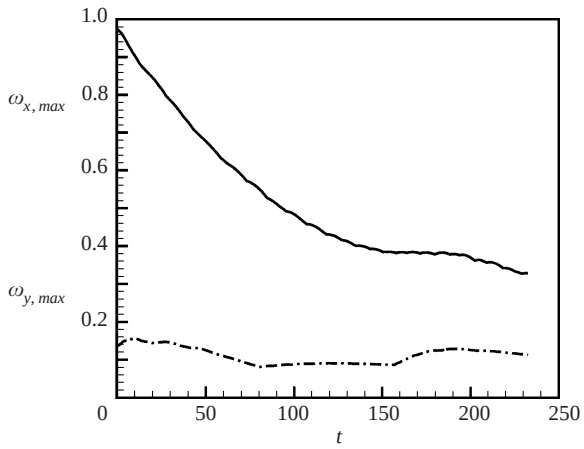

FIGURE 23. Time variation of the maximum vorticity values in the x- and y-directions for case D.

the limit of small Γ_2/Γ_1, it is mainly the self-induced velocity of the weak vortex that is responsible for driving the two vortices together. This self-induced velocity is naturally reduced as the weak vortex strength is reduced. The strength of the weak vortex in the $x = 0$ symmetry plane approaches zero near the end of the computation.

Variation of the maximum vorticity components in the x- and y-directions is plotted versus time in figure 23. The vorticity component in the x-direction decays steadily in time, with only a gradual flattening during the vortex interaction. The y-component of vorticity is nearly constant in time.

We thus see that for moderate and small values of Γ_2/Γ_1, the rate of stretching of the weak vortex decreases with decrease in Γ_2/Γ_1, which occurs because the self-induced velocity of the weak vortex, which is primarily responsible for driving the vortex cores together, is proportional to the weak vortex strength. Stretching causes the vorticity within the weak vortex core to increase, thus decreasing the ratio of transverse straining rate (induced by the strong vortex) to vorticity within the weak vortex core. Decrease in Γ_2/Γ_1 thus leads to increased deformation of the weak vortex core.

The vorticity response within the strong vortex can be examined by plotting the x and y vorticity components in the cross-plane $y = -0.7$ at time $t = 231$ (figure 24), which slices down the middle of the strong vortex. The contours with negative values are shaded, so the regions of the cross-plane occupied by the weak and strong vorticies can be identified from the plot of ω_x contours in figure 24(a). The ω_y contours in figure 24(b) exhibit alternating signs as we proceed vertically from top to bottom, similar to that observed for case C (figure 16).

The mechanism for generation of azimuthal vorticity within the strong vortex may be understood by considering an axisymmetric model problem, consisting of a columnar vortex centred on the symmetry axis that is enclosed by a series of periodic vortex rings of alternating signs. The velocity induced by the vortex rings cause a periodic axial stretching and compression of the columnar vortex core, resulting in alternating bulging and thinning of the core, as sketched in figure 25. Associated with this bulging and thinning is a radial tilting of the predominately axial vorticity within the columnar vortex core, where the vorticity vectors on the lateral surface of the core follow the slope of the core boundary. The inviscid vorticity transport equation

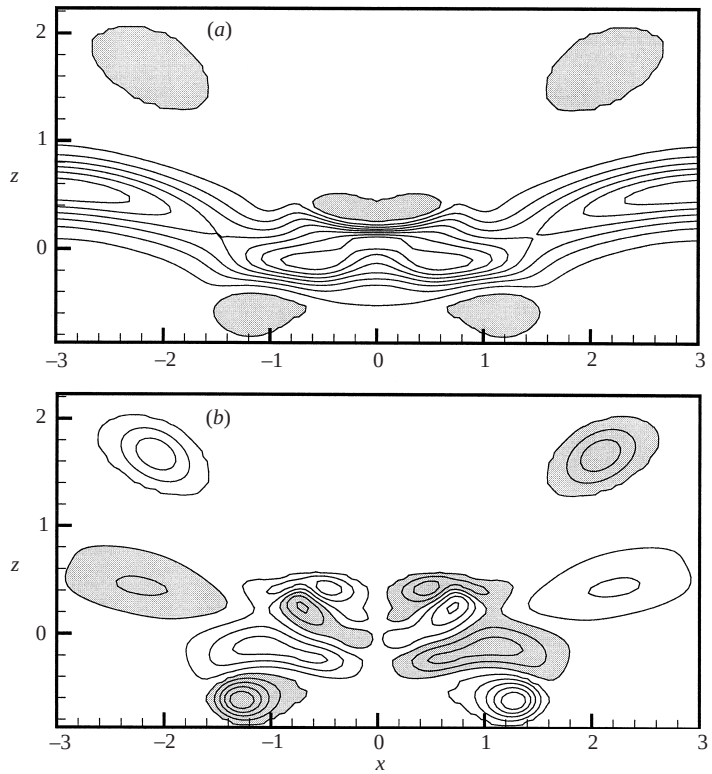

FIGURE 24. Contours of (*a*) ω_x and (*b*) ω_y over a planar cut at $y = -0.7$ for case D at time $t = 231$. Contours with negative values are shaded.

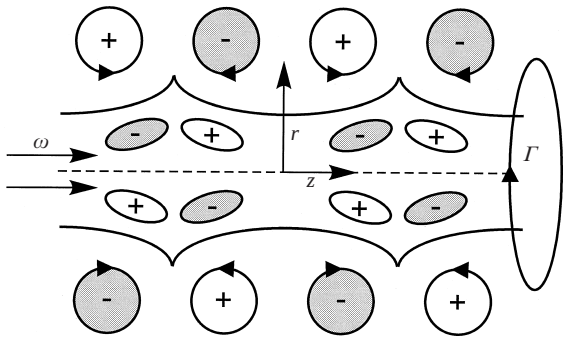

FIGURE 25. Schematic diagram illustrating the mechanism of azimuthal vorticity generation within the core of a columnar vortex owing to axial stretching and compression induced by wrapped vorticity structures.

for the azimuthal vorticity in an axisymmetric flow can be expressed as (Saffman 1992)

$$\frac{\mathrm{D}}{\mathrm{D}t}\left(\frac{\omega_\theta}{r}\right) = -\frac{2u_\theta\omega_r}{r^2}, \tag{4}$$

where $\mathrm{D}/\mathrm{D}t$ is the material derivative and (r, θ, z) are cylindrical polar coordinates.

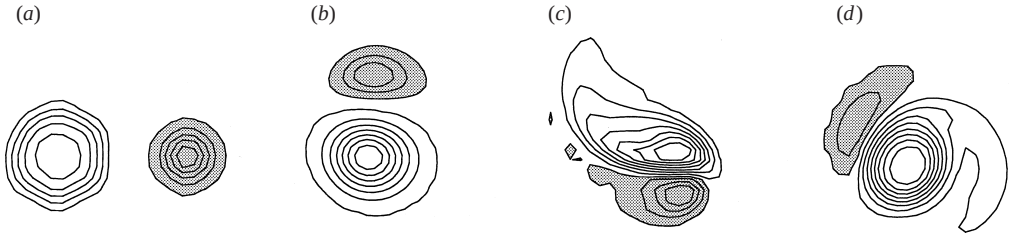

FIGURE 26. Vorticity contours in the $x = 0$ symmetry plane, for the same times as shown in figure 19, for case E. Contours with negative values are shaded.

Using the vorticity definition in an axisymmetric flow, (4) can be written alternatively as

$$\frac{\mathrm{D}\omega_\theta}{\mathrm{D}t} = \frac{u_r\omega_\theta}{r} + r\left[\omega_r\frac{\partial}{\partial r}\left(\frac{u_\theta}{r}\right) + \omega_z\frac{\partial}{\partial z}\left(\frac{u_\theta}{r}\right)\right]. \tag{5}$$

The first term on the right-hand side of (5) represents stretching of existing azimuthal vorticity by the radial velocity and the second term (which is equal to the right-hand side of (4)) represents generation of new azimuthal vorticity by tilting of the radial and axial vorticity components in the azimuthal direction owing to radial and axial gradients, respectively, of the angular rotation rate u_θ/r. Equation (4) indicates that positive azimuthal vorticity is generated in locations with negative radial vorticity and vice versa, resulting in an alternating distribution of azimuthal vorticity within the columnar vortex of opposite sign to that of the nearby wrapped vortex structure, as represented by the patches of positive and negative azimuthal vorticity within the columnar vortex core in figure 25. In the computational vorticity contours shown in figure 24(*b*), the vorticity generated by this radial tilting mechanism is superimposed on that associated with the slight bending of the strong vortex. Nevertheless, the mechanism described above is primarily responsible for the generation of vorticity that allows the strong vortex to resist the axial straining induced by the wrapped weak vortex structure.

One potential application of this research is the control of strong vortex structures by injection of weaker nearby vortices. For such applications to be practical, it is usually required that the weaker vortex has a strength that is much less than that of the stronger vortex. The computations reported in the current paper indicate no dramatic breakup of the strong vortex caused by interaction with much weaker vortices for cases where the two vortex structures have nearly the same core radius. In cases with very different core radii, the vorticity within the weak vortex may be comparable to or higher than that within the strong vortex, which would make the weak vortex more resistant to straining and more able to strip vorticity from the strong vortex core. To examine the effect of unequal core radii, the computation with $\Gamma_2/\Gamma_1 = 0.25$ is repeated for a case with $\sigma_2/\sigma_1 = 0.5$ (case E), such that the initial maximum vorticity within the two structures is approximately equal. The weak vortex is observed to wrap around the stronger vortex at approximately the same rate as observed in figure 19. The vorticity contours in the $x = 0$ symmetry plane are plotted in figure 26, and an iso-surface of vorticity magnitude at time $t = 231$ is plotted in figure 27. The vorticity contours in the symmetry plane exhibit strong core deformation of both vortex structures as the weaker vortex moves towards and wraps around the stronger vortex. Eventually, the weak vortex is depleted by cross-

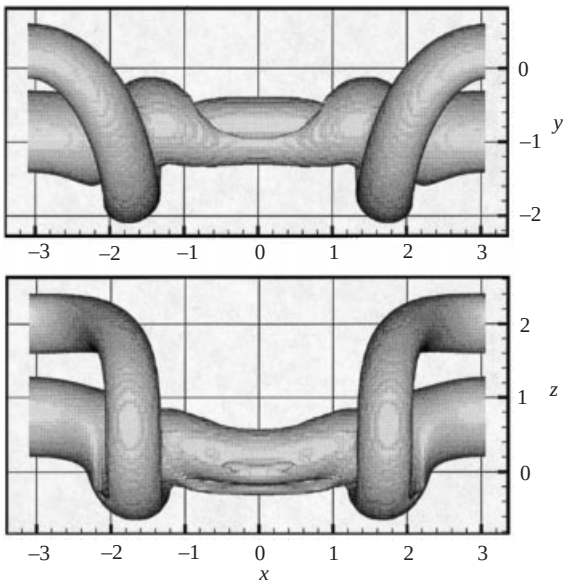

FIGURE 27. Iso-surface of vorticity magnitude for case E at time $t = 231$, showing projections in the (x, y)- and (x, z)-planes.

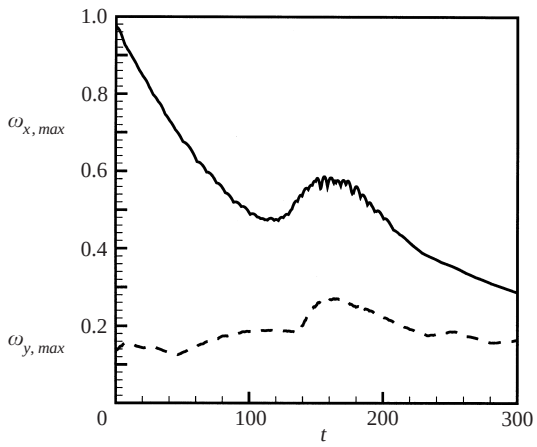

FIGURE 28. Time variation of the maximum vorticity values in the x- and y-directions for case E.

diffusion to such an extent that it becomes unstable to two-dimensional straining, and consequently is stretched into an elongated shape. The strong vortex rolls back up into a nearly circular shape at long time, with a tail of ejected vorticity spiralling behind.

Another difference between the flows with equal vortex cores (case D) and that with unequal core radii (case E) can be observed by comparing the time variation of vorticity components in the x- and y-directions, plotted in figures 23 and 28. The maximum value of ω_x first decays and then peaks at a time of about 170 in the unequal core radii case (E), with a more gradual peak in ω_y at nearly the same time. This increase in the maximum vorticity value is indicative of significant stretching within the strong vortex owing to the wrapped weak vortex structure. By contrast,

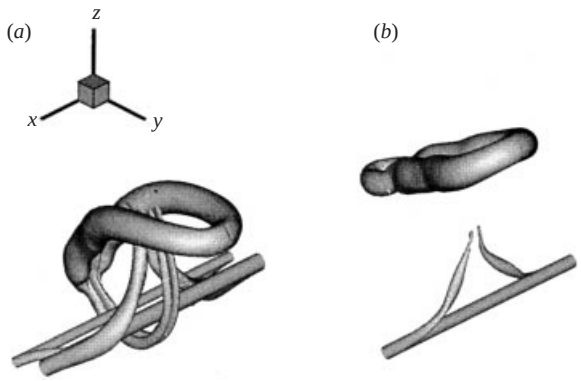

FIGURE 29. Iso-surfaces of λ_2 for case B at times (*a*) $t = 415$, (*b*) $t = 622$.

the maximum value of ω_x decays monotonically in time for the equal-core case (D), suggesting that vortex stretching has a much less significant role.

7. Long-time vortex evolution

Sections 4–6 show that when an anti-parallel vortex pair is driven together by the vortex mutual instability, the vorticity field separates into two regions. One of these regions forms from the vorticity 'bridges' spanning between the two structures. Neighbouring bridges propagate toward each other owing to the self-induced velocity caused by the curvature associated with wrapping of the weak vortex around the strong vortex, eventually pinching off to form a loop formed of vorticity originating half from the weak vortex and half from the strong vortex. The second vorticity region consists of the 'threads' or remnants of the vortices that are left behind. The strength of the loop formed by the bridges must be equal to or less than that of the weak vortex, and the net circulation about the threads must be equal to or less than the difference between the strong and weak vortex strengths. The current section examines the long-time evolution of these two vorticity regions for a case with slight vortex strength difference (case B) and another with large strength difference (case D).

For slight strength differences, the thread region is weak and hence not able to exert much influence on the motion of the loop formed from the bridges. The self-induced velocity of these loops causes them to eventually advect away from the threads, while the threads remain approximately fixed in space and roll up over long time into a weak columnar vortex. A plot of a λ_2 iso-surface showing this behaviour for case B is given in figure 29 for times $t = 415$ and 622. The figure has been rearranged to focus on the vortex loop by translating half of the flow domain one period length in the positive x-direction. Figure 29(*a*) shows the different orientations of vortex filaments that are produced when the loop formed from the bridges tears away from the initial columnar vortices. These filaments die away with time owing to cross-diffusion, so that after the vortex loop has propagated some distance away (figure 29*b*) the remaining vorticity progressively rolls up into a columnar vortex.

For large strength differences, the vortex loop formed from the bridge regions is weak compared to the remaining vorticity within the strong vortex, which has an approximately columnar form. The vortex loop is therefore not able to escape, but instead wraps around the strong vortex as shown in figure 30. The self-induced velocity of the vortex loop, due to the curvature induced by wrapping around the

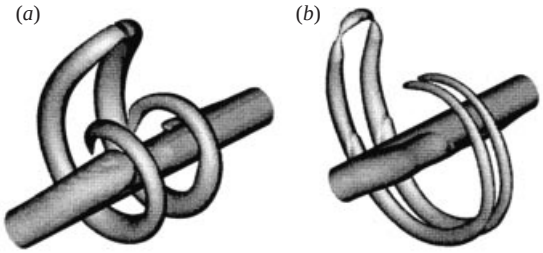

FIGURE 30. Iso-surfaces of λ_2 for case D at times (*a*) $t = 461$, (*b*) $t = 769$.

strong vortex, causes the two legs of the loop to propagate toward each other (figure 30*a*). The vortex loop thus evolves into a tight hairpin (figure 30*b*), while at the same time advecting radially outward from the strong vortex owing to the mutually induced velocity between the two vortex legs. The stretching associated with outward radial motion causes a decrease in the core radius of the loop.

8. Conclusions

A study is reported which examines the effect of unequal vortex strength on the interaction of nominally anti-parallel vortex tubes that are driven together by the three-dimensional vortex pair instability. The effect of unequal vortex strength on the vortex reconnection phenomenon is examined using a series of computations for vortices with equal initial core radius but different strengths. The difference in vortex strength breaks the symmetry over the (x, z)-plane, resulting in wrapping of the weak vortex around the strong vortex.

The vortex interaction is dominated by a combination of vorticity cross-diffusion (with the associated bridging of vorticity between the two structures) and deformation of the vortex cores caused by the mutual straining between the two vortices. In all cases considered, the weak vortex attaches to the strong vortex in a series of loops, which are connected by the remnants of the weak and strong vortices. The vorticity structure within these remnants depends on the difference in vortex strength. For cases with slight vortex strength difference, the stretching associated with the wrapping process sufficiently enhances the vorticity within the core of the weak vortex that the remnant of the weak vortex is able to remain roughly circular during the later stages of the reconnection process, while the strong vortex core is deformed into an elongated sheet. For moderate vortex strength differences, both the weak and strong vortex cores are deformed during the interaction, whereas for large strength differences only the weak vortex core is significantly deformed. Decrease in core radius of the weak vortex is shown to make the weak vortex more resistant to straining and better able to strip vorticity from the strong vortex. For cases with large vortex strength difference, the weak vortex wraps around the strong vortex with only small deflection of the strong vortex. The radial tilting of vorticity within the strong vortex core, induced by the wrapped loops of the weak vortex, induces formation of an interlaced pattern of positive and negative vorticity spirals within the strong vortex core.

Over long time, the bridge regions tear away from the columnar vortices to form loops composed of vorticity originating from both the weak and strong vortices. For slight vortex strength difference, the threads are weak relative to the loops, so that over time the loops propagate away leaving the threads behind. For large strength

difference, the loops are weak relative to the strong vortex, which remains nearly columnar as the loops wrap around it.

Future work might consider the effect of increased Reynolds number on the vortex interaction. Although the Reynolds number used in this paper may be characteristic of interaction of coherent vortices in engineering-scale turbulent flows with smaller-scale turbulence, it is much smaller than would typically be observed for large-scale vortex flows, such as aircraft wake vortices. In cases with higher Reynolds number, the weak vortex will wrap a larger number of times around the strong vortex, and hence experience more stretching and reduction in core radius, prior to significant formation of bridges connecting the weak and strong vortices. Stretching enhances the core vorticity of the weak vortex (for a given vortex strength), thereby enhancing the ability of the weak vortex to strip vorticity from the strong vortex core. Unfortunately, significantly higher Reynolds numbers and larger differences in vortex core radii introduce severe challenges for numerical computation.

Funding was provided to J. S. M. during his leave at IMFT by the French Ministry of Education. Computer time was provided by a grant from the National Partnership for Advanced Computational Infrastructure, San Diego, California.

REFERENCES

Acarlar, M. S. & Smith, C. R. 1987 A study of hairpin vortices in a laminar boundary layer. Part 2. Hairpin vortices generated by fluid injection. *J. Fluid Mech.* **175**, 43–83.

Bandyopadhyay, P. R., Stead, D. J. & Ash, R. L. 1991 Organized nature of a turbulent trailing vortex. *AIAA J.* **29**, 1627–1633.

Corsiglia, V. R. & Dunham, R. E. 1976 Aircraft wake–vortex minimization by use of flaps. *Wake Vortex Minimization*, NASA SP-409.

Croom, D. R. 1976 The development and use of spoilers as vortex attenuators. *Wake Vortex Minimization*, NASA SP-409.

Crow, S. C. 1970 Stability theory for a pair of trailing vortices. *AIAA J.* **8**, 2172–2179.

Jeong, J. & Hussain, F. 1995 On the identification of a vortex. *J. Fluid Mech.* **285**, 69–94.

Kerr, M. & Hussain, F. 1989 Simulation of vortex reconnection. *Physica* D **37**, 474–484.

Kida, S. & Takaoka, M. 1994 Vortex reconnection. *Ann. Rev. Fluid Mech.* 26, 169–189.

Klein, R., Majda, A. J. & Damodaran, K. 1995 Simplified equations for the interaction of nearly parallel vortex filaments. *J. Fluid Mech.* **288**, 201–248.

Krishnamoorthy, S. & Marshall, J. S. 1998 Three-dimensional blade–vortex interaction in the strong vortex regime. *Phys. Fluids* **10**, 2828–2845.

Liu, H. T. 1992 Effects of ambient turbulence on the decay of a trailing vortex wake. *J. Aircraft* **29**, 255–263.

Marshall, J. S. 1997 The flow induced by periodic vortex rings wrapped around a columnar vortex core. *J. Fluid Mech.* **345**, 1–30.

Melander, M. V. & Hussain, F. 1989 Cross-linking of two anti-parallel vortex tubes. *Phys. Fluids* A **1**, 633–635.

Melander, M. V. & Hussain, F. 1993 Coupling between a coherent structure and fine-scale turbulence. *Phys. Rev.* E **48**, 2669–2689.

Melander, M. V. & Zabusky, N. J. 1988 Interaction and 'apparent' reconnection of 3D vortex tubes via direct numerical simulations. *Fluid Dyn. Res.* **3**, 247–250.

Moore, D. W. & Saffman, P. G. 1971 Structure of a line vortex in an imposed strain. *Aircraft Wake Turbulence and its Detection*, pp. 339–354. Plenum.

Pumir, A. & Kerr, R. M. 1987 Numerical simulation of interacting vortex tubes. *Phys. Rev. Lett.* **58**, 1636–1639.

Quackenbush, T. R., Batcho, P. F., Bilanin, A. J. & Carpenter, B. F. 1998 Design, fabrication and test planning for an SMA-activated vortex wake control system. *Proc. SPIE* **3326**, 259–271.

Quackenbush, T. R., Bilanin, A. J., Batcho, P. F., McKillip, R. M. & Carpenter, B. F.

1997 Implementation of vortex wake control using SMA-activated devices. *Proc. SPIE* **3044**, 134–146.

Saffman, P. G. 1990 A model of vortex reconnection. *J. Fluid Mech.* **212**, 395–402.

Saffman, P. G. 1992 *Vortex Dynamics*, p. 71. Cambridge University Press.

Siggia, E. D. 1985 Collapse and amplification of a vortex filament. *Phys. Fluids* **28**, 794–805.

Shelley, M. J., Meiron, D. I., & Orszag, S. A. 1993 Dynamical aspects of vortex reconnection of perturbed anti-parallel vortex tubes. *J. Fluid Mech.* **246**, 613–652.

Takai, R. & Hussain, F. 1985 Recombination of vortex filaments and its role in aerodynamic noise. *Turbulent Shear Flow V* (ed. F. Durst, B. E. Launder, J. L. Lumley, F. W. Schmidt & J. H. Whitelaw), pp. 3.19–3.25. Springer.

Tombach, I. 1973 Observations of atmospheric effects on vortex wake behavior. *J. Aircraft* **10**, 641–646.

Zabusky, N. J. & Melander, M. V. 1989 Three-dimensional vortex tube reconnection: morphology for orthogonally-offset tubes. *Physica* D **37**, 555–562.